

Lithium anode interlayer design for all-solid-state lithium-metal batteries

Received: 1 March 2023

Accepted: 30 November 2023

Published online: 08 January 2024

 Check for updates

Zeyi Wang¹, Jiale Xia¹, Xiao Ji¹, Yijie Liu¹, Jiaxun Zhang¹, Xinzi He¹,
Weiran Zhang², Hongli Wan¹✉ & Chunsheng Wang¹✉

All-solid-state lithium-metal batteries (ASSLBs) have attracted intense interest due to their high energy density and high safety. However, Li dendrite growth and high interface resistance remain challenging due to insufficient understanding of the mechanism. Here we develop two types of porous lithiophobic interlayer ($\text{Li}_7\text{N}_2\text{I}$ -carbon nanotube and $\text{Li}_7\text{N}_2\text{I}$ -Mg) to enable Li to plate at the Li/interlayer interface and reversibly penetrate into the porous interlayer. The experimental and simulation results reveal that a balance of lithiophobicity, electronic and ionic conductivities and interlayer's porosity are the key enablers for stable Li plating/stripping at a high capacity. A fine-tuned $\text{Li}_7\text{N}_2\text{I}$ -carbon nanotube interlayer enables Li/LNI/Li symmetric cell to achieve a high critical current density of 4.0 mA cm^{-2} at 4.0 mAh cm^{-2} at 25°C ; the $\text{Li}_7\text{N}_2\text{I}$ -Mg interlayer enables a $\text{Li}_4\text{SiO}_4@\text{LiNi}_{0.8}\text{Mn}_{0.1}\text{Co}_{0.1}\text{O}_2/\text{Li}_6\text{PS}_5\text{Cl}/20 \mu\text{m-Li}$ full cell to achieve an areal capacity of 2.2 mAh cm^{-2} , maintaining 82.4% capacity retention after 350 cycles at 60°C at a rate of 0.5 C. The interlayer design principle opens opportunities to develop safe and high energy ASSLBs.

An all-solid-state battery with a lithium-metal anode is a promising candidate for electric vehicles due to its higher energy density and safety^{1–5}. Solid-state electrolytes (SSEs) possess several intrinsic advantages compared with traditional liquid electrolytes. First, the solid electrolyte is less flammable than liquid electrolytes, making the battery much safer^{4,5}. Second, SSEs with a unit Li ion transference number could evade the concentration gradient-induced Li dendrite growth, enhancing the charge/discharge power density⁶. Finally, a high mechanical strength of $>7\text{--}8 \text{ GPa}$ of the solid electrolytes is expected to block the lithium dendrite penetration, achieving high energy density and long cycle life^{7,8}.

However, extensive research demonstrated that Li dendrite growth in all-solid-state lithium-metal batteries (ASSLBs) is easier than that in batteries with liquid electrolytes^{9,10} and the governing mechanism for Li dendrite growth in ASSLBs remains a mystery^{11–16}. The Li dendrite can grow either from the Li anode into the electrolyte (outside in)^{7,11} or directly nucleate inside the electrolyte and grow to the outside electrode (inside out)^{12,13}. Increasing the electrolyte lithiophobicity and reducing the electronic conductivity can effectively suppress the Li nucleation inside electrolytes, thus preventing the inside-out Li

dendrite growth^{12,13}. For outside-in Li dendrite growth, many efforts aim to enhance the mechanical strength, uniformity and density of the solid electrolyte⁷. However, the attempts at densification¹⁷, amorphization¹⁰ and single crystallization¹⁰ have demonstrated a failure to block the outside-in Li dendrite growth. Because the mechanical property of the solid electrolytes is greatly changed by the chemical and electrochemical reaction with Li anode, more research on enhancing the chemical and electrochemical stability of solid electrolytes was conducted^{15,16}.

$\text{Li}_7\text{La}_3\text{Zr}_2\text{O}_{12}$ (LLZO) is more stable with Li than Li_3PS_4 (LPS) and Li_3YCl_6 (LYC) electrolytes and is usually applied as a model electrolyte to investigate the mechanism of Li plating. However, an electrochemical reaction still takes place between LLZO and Li at a negative potential due to a large Li plating overpotential¹⁵. The reduction reactions between Li and electrolyte inject electrons into the electrolyte and induce phase changes, which not only generate internal stress and cracks inside the electrolyte but also destroy the Li-ion conduction channel promoting Li dendrite growth. The Li dendrite growth in LPS and LYC is more pronounced due to less stability against Li¹⁶. Exploring new solid electrolytes that are thermodynamically stable

¹Department of Chemical and Biomolecular Engineering, University of Maryland, College Park, MD, USA. ²Department of Materials Science and Engineering, University of Maryland, College Park, MD, USA. ✉ e-mail: hwan@umd.edu; cswang@umd.edu

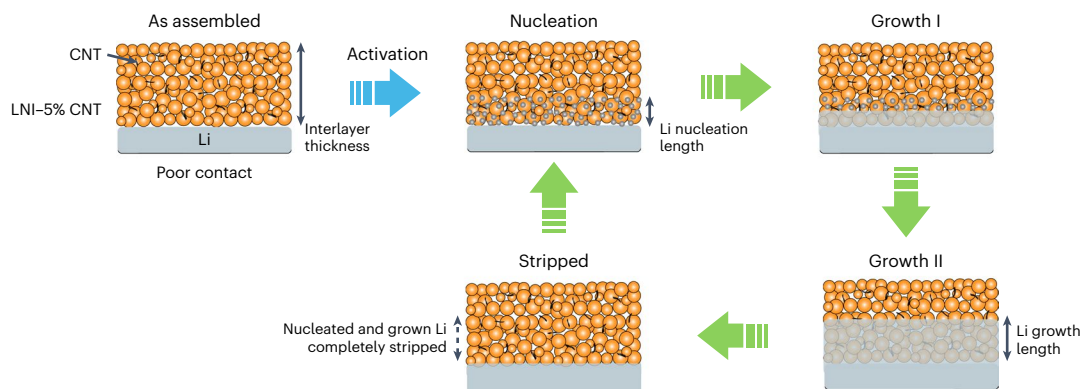


Fig. 1 | The evolution of Li/interlayer interface after cells assemble, Li nucleation, Li growth and Li stripping. The grey rectangle is the Li anode. The yellow spheres are LNI electrolyte particles. The small grey spheres are nucleated Li. The black sticks are CNT. The Li/LNI-5% CNT interface has poor contact in an assembled Li/LNI/Li cell. After activation, Li can nucleate on the Li/LNI-CNT

interface (rather than the SSE/LNI-CNT interface) and then reversibly penetrate into/extract from the porous LNI-CNT interlayer during Li plating/stripping. If the Li growth length is larger than the Li nucleation length, the nucleus was merged during Li plating and was completely extracted during Li stripping.

to Li is urgently needed for ASSLBs. In addition to the mechanical and chemical/electrochemical properties of solid electrolytes, the void is also formed at the interface between Li and solid electrolyte during Li stripping when the Li stripping rate is higher than the Li replenishing rate¹⁸, which increases the overpotential of the cell promoting the electrolyte reduction and Li dendrite growth¹⁴.

To avoid electrolyte reduction and void formation, solid electrolyte interlayers with different ionic and electronic conductivity, lithiophobicity were inserted between Li and solid electrolytes. Electronic conductive and lithiophilic interphase such as Au¹⁹, Al^{19,20}, Sn²¹ were used to suppress void formation. However, the high electronic conductivity of the interphase/interlayer also accelerates the electrolyte reduction during Li plating. Using lithiophobic and/or highly ionic conductive interlayers such as Li₃OCl (ref. 22), LiF (ref. 23) and LiF-Li₃N (ref. 24) can suppress electrolyte reduction but promote void formation due to low Li diffusivity. A recently reported porous lithiophobic/lithiophilic gradient interlayer^{25,26} was found to simultaneously suppress the void formation and electrolyte reduction if the interlayer has a low electronic conductivity, high ionic conductivity and is lithiophobic, enabling Li deposits at the interface of interlayer/Li rather than inside interlayer and on the solid electrolyte surface. However, if the interlayer is lithiophilic and has high electronic conductivity but a low ionic conductivity, Li will deposit inside the interlayer and on the solid electrolyte surface reducing the solid electrolytes. The relationship among lithiophobicity, electronic/ionic conduction properties of interlayers and Li dendrite suppression capabilities has not been systematically investigated yet but is critical for ASSLBs.

In this work, by adjusting the property of the Li₂N₂I-carbon nanotube (LNI-CNT) interlayer and LNI-Mg interlayer, we correlated Li plating stability with ionic and electronic conductivities and lithiophobicity of the interlayer. LNI has a high ionic conductivity of $3.1 \times 10^{-4} \text{ S cm}^{-1}$ and a low electronic conductivity, high lithiophobicity and high electrochemical stability against Li, whereas CNT has a high lithiophobicity, high electronic conductivity and low tap density. Therefore, mixing LNI with CNT at different ratios can form porous lithiophobic interlayers with variable ionic and electronic conductivity. LNI-Mg interlayer can form gradient electronic conductivity inside the interlayer due to Mg migrating from the interlayer to the Li anode during activation, which can reduce the interlayer thickness and enhance the Li dendrite suppression capability. For LNI-CNT, the 90 μm LNI-5% CNT interlayer enabled Li to nucleate on the Li/LNI-CNT interface (rather than the SSE/LNI-CNT interface) and then reversibly penetrate into/extract from the porous LNI-CNT interlayer during Li plating/stripping (Fig. 1). The three-dimensional Li/LNI-5% CNT interlayer contact achieved

by well-controlled Li nucleation and growth enabled the Li/LNI/Li cell to charge/discharge at a high current density of 4.0 mA cm^{-2} and a high capacity of 4.0 mAh cm^{-2} for $>600 \text{ h}$. For the LNI-Mg interlayer, the gradient electronic conductivity in the 18.5 μm LNI-Mg interlayer enables Li₄SiO₄@LiNi_{0.8}Mn_{0.1}Co_{0.1}O₂/Li₆PS₃Cl/Li (LSO@NMC811/LPSC/Li) full cells with an areal capacity of 2.2 mAh cm^{-2} to be charged/discharged for 350 cycles at 60 °C with capacity retention of 82.4%. We also reported that stable Li plating/stripping cycle can be achieved if the Li nucleation region in the interlayer is smaller or equal to the Li growth region in the interlayer (from the Li anode), which is verified by tuning the ratio of LNI and CNT in the interlayer (Fig. 1). This study represents a comprehensive interlayer design for ASSLBs with a notably improved dendrite suppression capability and reversibility.

Impact of interlayer properties on Li plating

An LNI solid electrolyte was synthesized following the procedure reported in Supplementary Note 1 (Supplementary Figs. 1–5). LNI solid electrolyte is thermodynamically stable to Li (Supplementary Fig. 2) and has high interface energy against Li metal (Supplementary Fig. 3). By mixing LNI with lithiophobic CNT, (Supplementary Note 2 and Supplementary Figs. 6 and 7), a porous LNI-CNT composite interlayer with tunable lithiophobicity and ionic/electronic conductivities was prepared (Supplementary Figs. 8 and 9) and was inserted between Li and LNI electrolytes to guide Li deposition only at the interlayer/Li (rather than at LNI/interlayer; Supplementary Fig. 10). Three LNI-CNT interlayers with CNT content of 0.5%, 5% and 50% were selected for investigation. The ionic and electronic conductivity of LNI-CNT interlayers were measured at room temperature (RT) using electrochemical impedance spectroscopy (EIS) and direct current (d.c.) polarization. The ionic and electronic conductivity are $3.0 \times 10^{-4} \text{ S cm}^{-1}$ and $6.7 \times 10^{-8} \text{ S cm}^{-1}$ for LNI-0.5% CNT, $2.9 \times 10^{-4} \text{ S cm}^{-1}$ and $2.8 \times 10^{-5} \text{ S cm}^{-1}$ for LNI-5% CNT and $2.4 \times 10^{-5} \text{ S cm}^{-1}$ and $5.0 \times 10^{-2} \text{ S cm}^{-1}$ for LNI-50% CNT interlayers. Therefore, LNI-0.5% CNT, LNI-5% CNT and LNI-50% CNT interlayers are ionic conductors, mixed ionic-electronic conductors and electronic conductors, respectively (Supplementary Note 3 and Supplementary Figs. 11 and 12).

The impact of LNI-x% CNT interlayer (90 μm) on Li plating/stripping stability was investigated in Li/LNI/Li symmetric cells, where LNI electrolyte was sandwiched by two LNI-x% CNT ($x = 0.5, 5, 50$) interlayers (Supplementary Fig. 10). The Li/LNI-CNT/LNI/LNI-CNT/Li cells were charged/discharged at a small current density of 0.1 mA cm^{-2} with a capacity of 0.1 mAh cm^{-2} . As we can see from Fig. 2a, cells with LNI-0.5% CNT interlayers show a stable and flat voltage profile with an overpotential of -0.27 V along cycles. LNI-5% CNT sandwiched cells (Fig. 2b) initially have a large overpotential of 0.3 V and its overpotential gradually

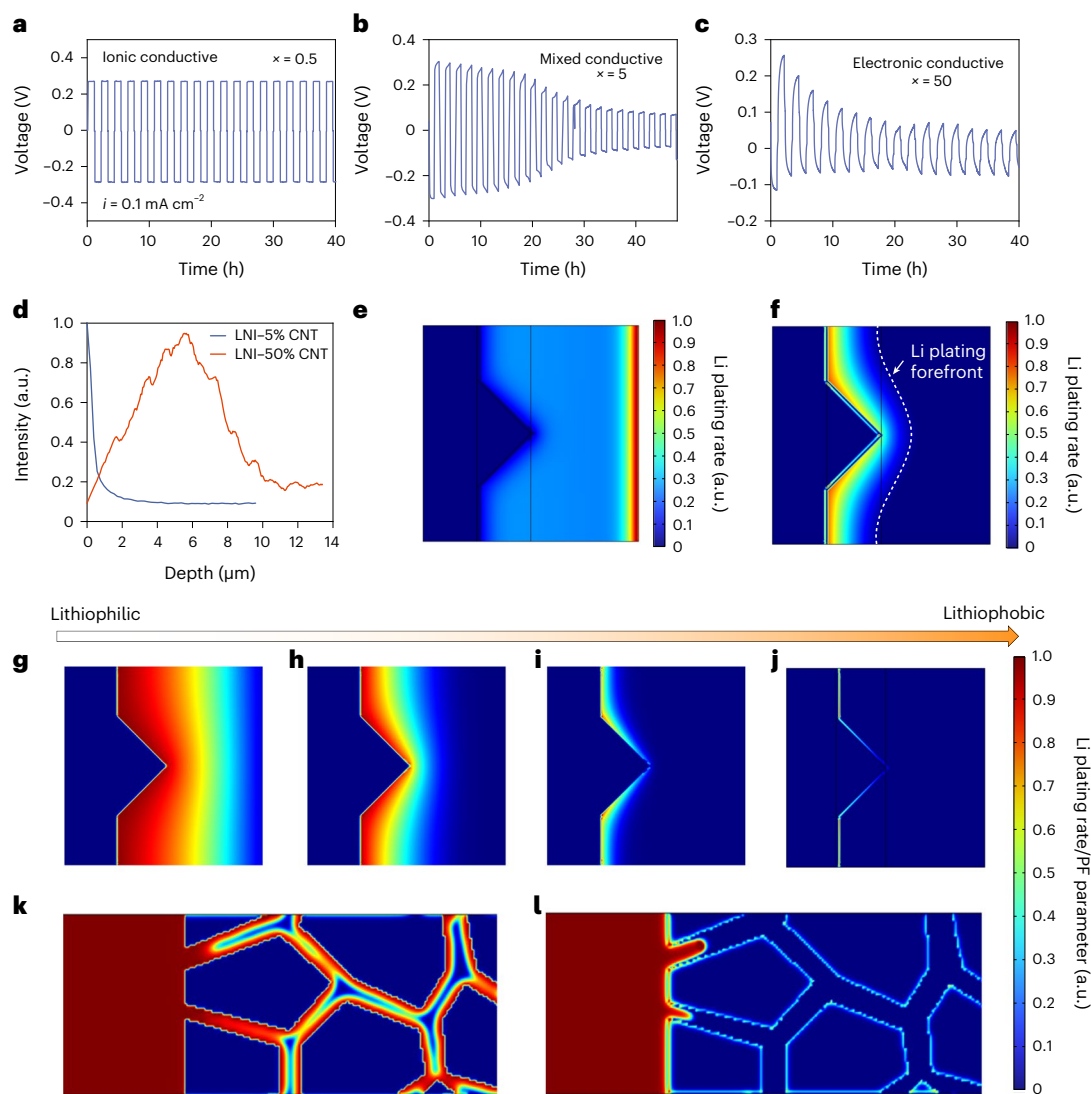


Fig. 2 | Li stripping/plating behaviours in ionic conductive, mixed conductive and electronic conductive interlayers. **a–c**, Voltage profile of Li/LNI/Li symmetric cells sandwiched with LNI- $x\%$ CNT composites at a current density of 0.1 mA cm^{-2} with a capacity of 0.1 mAh cm^{-2} when $x = 0.5$ (**a**), $x = 5$ (**b**) and $x = 50$ (**c**). **i** in the Fig. **a** is current density. The voltage drops in Li/LNI/Li symmetric cells with LNI-5% CNT and LNI-50% CNT interlayers were attributed to Li plating into interlayers. The Li nucleation peaks were not observed because they were covered by the high Li stripping overpotential of Li counter electrodes before fully activation. **d**, ToF-SIMS analysis of the Li distribution on LNI-0.5% CNT and

LNI-50% CNT interlayers along the depth of the sputtered crater. **e, f**, Simulated Li growth and nucleation in electronic conductive (**e**) and mixed conductive interlayers (**f**). **g–j**, Spatial distribution of Li nucleation in interlayers with enhanced lithiophobicity from left to right. The growth and nucleation rate were normalized to the range of 0 to 1. **k, l**, Li growth at lithiophilic interlayers (**k**) and lithiophobic interlayers (**l**) using phase field models. The colour map represents the normalized Li nucleation rate or phase field (PF) parameter. Phase field parameter of 1 is Li metal.

decreases and is finally stable at -0.07 V after 20 cycles. For LNI-50% CNT, the voltage drops from -0.25 V to -0.05 V in ten cycles (Fig. 2c). The overpotential decrease for the LNI-5% CNT interlayer was attributed to the Li growth into the interlayer, which was verified by a dramatic decrease in lithium signal intensity with a depth $< 2 \mu\text{m}$ and flattened at depths between 2 and $10 \mu\text{m}$ (Fig. 2d and Supplementary Fig. 13). The excess Li signal at depth $< 2 \mu\text{m}$ is attributed to Li plating into the porous LNI-5% CNT interlayer (Supplementary Fig. 13d). For Li/LNI/Li with electronic conductive LNI-50% CNT interlayers, lithium plates in entire electronic conductive LNI-50% CNT interlayers, as shown in lithium distribution curves and SEM observation (Fig. 2d and Supplementary Fig. 13b), which enhance the electronic conductivity of the interlayer and reduce the overpotential during galvanostatic cycles (Fig. 2c).

Li can simultaneously grow from Li anode into a porous LNI-CNT interlayer and can also directly nucleate in the interlayer depending on the ionic and electronic conductivity and lithiophobicity of the

LNI-CNT interlayer^{27,28}. To further understand Li plating behaviours in mixed ionic/electronic conductive interlayers, mathematical models were set up to simulate the Li growth from Li anode into interlayer and Li nucleation inside the interlayer (Supplementary Note 4, Supplementary Figs. 14–17 and Supplementary Tables 1 and 2). The Butler–Volmer equation²⁹ and classical nucleation theory^{28,30} were coupled with transport equations of electron and Li^+ ion to describe Li growth from Li anode into interlayer and nucleation in the interlayer (‘Li-ion and electron transport in mixed conductive interlayer’ in Methods section provides details). To account for the boundary of Li in the porous interlayer, the configuration of the model was set as Li growth with a triangle-shaped protrusion in contact with the interlayer (Supplementary Fig. 14). The simulation shows that Li nucleation in mixed conductive LNI-5% CNT interlayer generates a flat plating forefront for Li plating (Fig. 2f and Supplementary Fig. 16c) in sharp contrast to the uncontrolled Li nucleation in the entire electronic conductive LNI-50% CNT interlayer (Fig. 2e

and Supplementary Fig. 16b) and Li growth on the dendrite tip in ionic conductive LNI–0.5% CNT interlayer (Supplementary Fig. 16a).

The Li nucleation in the interlayer and Li growth into the interlayer (Supplementary Note 5 and Supplementary Figs. 18–20) also well explains the galvanostatic activation process of the Li/LNI/Li cell with LNI–CNT interlayer (Fig. 2a–c). The overpotential of Li/Li symmetric cells with LNI–0.5% CNT interlayer remains high and unchanged during activation (Fig. 2a) because Li does not nucleate in the LNI–0.5% CNT interlayer (Supplementary Fig. 18a–d). For Li/LNI/Li cell using LNI–5% CNT interlayer, the overpotential gradually reduces from 0–40 h and then remains nearly constant after 30 h of galvanostatic cycling (Fig. 2b) due to reversibly and stable Li penetration into/extraction from LNI–5% CNT interlayer (Supplementary Fig. 18e–h). However, for Li/LNI/Li symmetric cells with LNI–50% CNT interlayer (Fig. 2c), voltage rapidly drops within ten Li stripping/plating cycles owing to Li nucleation inside the entire interlayer including electrolyte surface (Fig. 2e and Supplementary Fig. 18i–l), which may lead to Li dendrite growth at the interlayer/SSE boundary (Supplementary Fig. 20).

In addition to electronic/ionic conductivity, lithiophobicity of the interlayer also substantially changes the Li growth from Li anode and nucleation inside the LNI–CNT interlayer. For lithiophilic interlayers, lithium nucleation sites are dispersive inside the interlayer as shown in Fig. 2g,h. Moreover, according to phase field models (Fig. 2k and Supplementary Table 3), Li tends to grow into the lithiophilic interlayer along cracks/holes due to capillary force. In contrast, Li cannot protrude into the lithiophobic interlayer unless a high pressure is applied at a high plating capacity because the capillary force generates a high pressure when Li penetrates into small holes/cracks (Fig. 2l and Supplementary Note 6). With enhanced lithiophobicity of the interlayers, Li critical nucleation overpotential η_c also increased and growth tends to confine in the area close to the Li anode/interlayer interface (Fig. 2i). When lithiophobicity of the interlayer is strong enough, that is, the applied overpotential η in the interlayer is less than critical nucleation overpotential η_c of interlayers, the Li nucleation will be completely suppressed (Fig. 2j). The absence of Li nucleation in mixed conductive lithiophobic interlayers has been observed experimentally in literature^{26,31,32}. For example, in a reported Ag/C interlayer²⁶, Ag migrates in the Ag/C interlayer to the Li anode side leaving carbon on the interlayer. By applying high stack pressure, the reported carbon-based interlayers were densified and the lithiophobicity of the interlayer can be fully exploited to suppress Li protrusion and Li nucleation in the carbon interlayer^{26,31,32}, which is consistent with our analytic prediction (Supplementary Fig. 21) and phase field simulations (Supplementary Fig. 22). In this work, the same effects for Li plating/stripping regulation were achieved by inserting a LNI–CNT interlayer with high ionic conductivity but a low electronic conductivity at the Li/SSE interface at low stack pressure (~1 MPa). The highly lithiophobic and porous LNI–CNT interlayer regulates the Li nucleation and growth to achieve reversible Li protrusion into/extraction from the interlayer (Supplementary Figs. 21 and 22). The influence of pore size and porosity on current distribution and Li deposition in the interlayer was considered. The simulation shows that a homogeneous current distribution at the Li/interlayer boundary can be achieved at a high current density for porous interlayers with small pores size (Supplementary Fig. 23 and Supplementary Note 7).

Briefly, mixed conductive, lithiophobic and porous LNI–5% CNT interlayer enables Li plate at the Li/LNI–5% CNT interlayer boundary to simultaneously avoid void formation and electrolyte reduction even at low stack pressure, which can fully unleash the Li dendrite suppression capability of the interface.

Li plating/stripping stability in LNI–CNT interlayer

The Li dendrite suppression capability of the Li/LNI–CNT/LNI/LNI–CNT/Li cells was evaluated at step-increased current densities at 25 °C after activation cycles. As shown in Supplementary Fig. 24, initially, the voltages

of Li/LNI/Li cells with LNI–0.5% CNT and LNI–50% CNT interlayers increased with currents. When the current increased to 0.16 mA cm⁻² and 0.62 mA cm⁻², respectively, both of the Li/LNI/Li cells experienced a dramatic voltage drop, indicating a short circuit due to the Li dendrite growth through the interlayer and LNI electrolyte. The EIS profiles of Li/LNI/Li cells with LNI–0.5% CNT and LNI–50% CNT interlayers before and after voltage drop also confirmed the short circuit with substantially reduced resistance from 2,600 to <40 Ω cm² for LNI–0.5% CNT and from 500 to 16 Ω cm² for LNI–50% CNT (Supplementary Fig. 24b,c,e,f)³³. For cells using LNI–5% CNT interlayer, the charge/discharge curve (Fig. 3a) can be divided into two distinct regimes. (1) A sharp voltage spike at the beginning of Li plating in each cycle due to Li nucleation in the interlayer (Fig. 3a,d,e). (2) Gradually raised voltage at the end of the stripping process attributed to reduced contact area at the Li/interlayer because Li was extracted from the porous interlayer. A critical current density (CCD) of >4.0 mA cm⁻² at a capacity of 4.0 mAh cm⁻² was achieved for Li/LNI/Li cells with LNI–5% CNT interlayers. The impedance of symmetric Li/LNI/Li cells with LNI–5% CNT interlayers before and after cycles at the current of 4.0 mA cm⁻² and capacity of 4.0 mAh cm⁻² are shown in Fig. 3b. The overpotential of the cells did not follow ohm law when the current density was stepwise increased (Fig. 3a) due to Li penetration into the pore of the interlayer (Supplementary Fig. 25 and Supplementary Note 8). During galvanostatic cycling at a step-increased current with a fixed time (Fig. 3a), Li plating capacity gradually increased and more Li penetrates into the porous LNI–5% CNT interlayer from the Li anode, which increases the contact area between Li and the interlayer. As a result, the total resistance of the Li symmetric cell decrease from the initial ~800 Ω (no Li growth into interlayer before Li plating) to ~150 Ω (4 mAh cm⁻² of Li growth into the pores of interlayer). The low interface resistance of the LNI–5% CNT interlayer in Li/LNI/Li cells is attributed to the mixed ionic–electronic conductive, and Li penetrates into the porous interlayer. The total resistance of the cell after cycling is still higher than the ohmic resistance of the LNI electrolyte without interlayers (~100 Ω, 400 μm of LNI electrolyte). The controllable and reversible Li growth into LNI–5% CNT interlayer will not cause Li dendrite growth and short circuit due to the high lithiophobicity of the interlayer, as further evidenced by the same shape and identical characteristic frequency in EIS indicating unchanged Li plating/stripping behaviour (Fig. 3b). Moreover, the EIS profile of the cycled cell shows an obvious diffusion region at a low frequency of 0.1 Hz, which also indicates that the Li growth into porous LNI–5% CNT interlayer and cell did not short by Li growth into the interlayer. Figure 3c demonstrates the cyclic performance of the Li/LNI–5% CNT/LNI/LNI–5% CNT/Li cell at a current density of 4.0 mA cm⁻² and a capacity of 4.0 mAh cm⁻². Figure 3d,e shows the enlarged time–voltage profile of Li/LNI–5% CNT/LNI/LNI–5% CNT/Li cells during cycles at 0–50 h and 500–550 h. No sudden voltage drop was observed during the cycles. It was also observed that the overpotential slightly decreases at the first 25 activation cycles before reaching stable due to the Li plating into the interlayer. X-ray powder diffraction (XRD) characterizations and Raman spectra after 300 cycles demonstrate that the chemical and phase structures of LNI remain stable during long-term cycling (Supplementary Fig. 26) because Li plates only on the Li/LNI–CNT interface rather than on the LNI surface. Moreover, the position and relative intensity of D peak and G peak does not change. An extra peak centred at 1,440 cm⁻¹ was detected from Raman spectra (Supplementary Fig. 26a), which can be attributed to a surface reduction (rather than bulk reaction) of CNT with Li³⁴. In the XRD pattern of cycled LNI–5% CNT interlayer for 300 cycles (Supplementary Fig. 26b), the extra peaks corresponding to Li metal were observed in the sample due to Li plating in the interlayer. Therefore, the reduction of resistance is not due to chemical/electrochemical reaction between Li and interlayers but is attributed to reversible Li penetration into/extraction from the porous interlayer as demonstrated previously (Fig. 2d,f). Taking advantage of reversible Li plating/stripping in mixed conductive interlayers, excellent performance at a high critical current density of

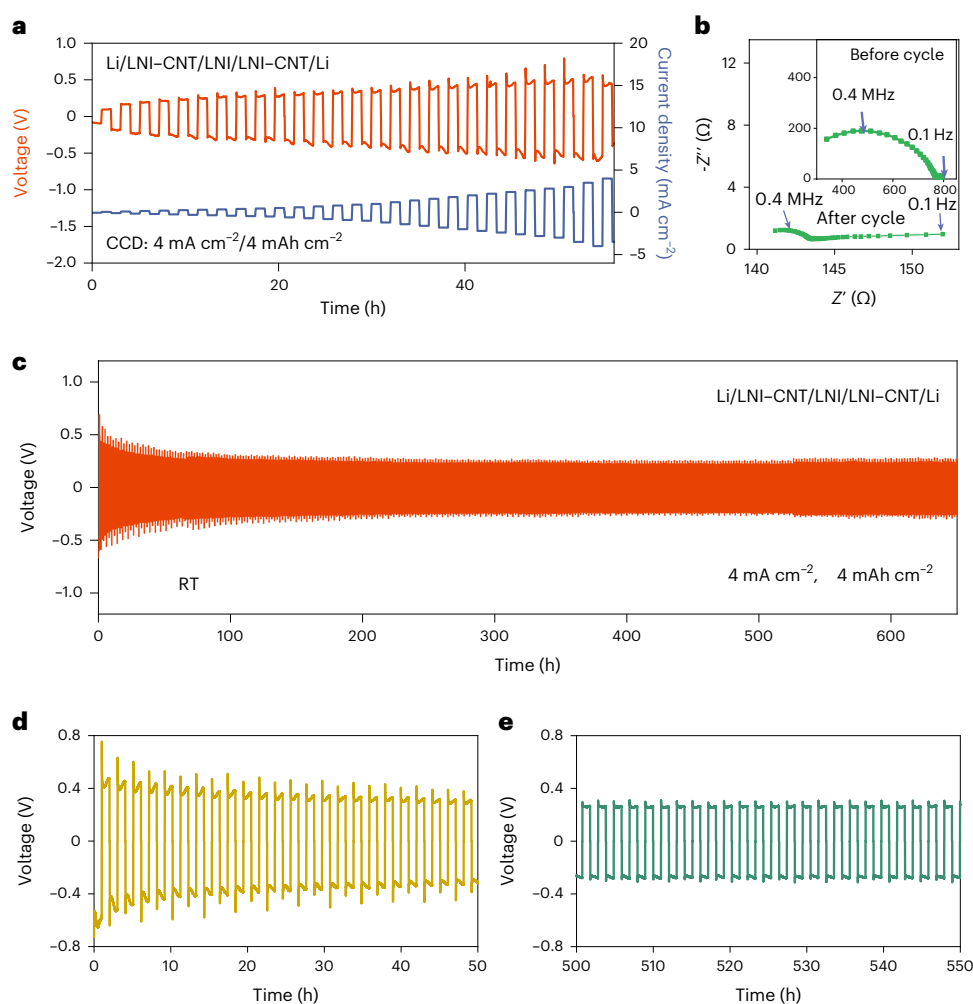


Fig. 3 | Li dendrite suppression capability of mixed conductive LNI-CNT interlayers. **a**, Galvanostatic cycling of Li/LNI/Li cells sandwiched with LNI-5% CNT interlayer at step-increased current densities at 25 °C. **b**, EIS of Li//Li cells using LNI electrolyte sandwiched with LNI-5% CNT composite before (inserted)

and after galvanostatic cycling. Z' and Z'' are real parts and imaginary parts of complex impedance, respectively. **c-e**, Voltage profiles of the Li/LNI-5% CNT/LNI/LNI-5% CNT/Li cell at 4.0 mA cm⁻² with a capacity of 4.0 mAh cm⁻² within 0-650 h (**c**), 0-50 h (**d**) and 500-550 h (**e**). RT is room temperature.

4.0 mA cm⁻² with a capacity of 4.0 mAh cm⁻² for over 600 h was achieved in Li/LNI-5% CNT/LNI/LNI-5% CNT/Li cell (Fig. 3c).

The criterion for stable Li plating in the interlayer

For a mixed conductive porous interlayer, both outside-in Li growth into the interlayer and inside-out Li nucleation in the interlayer simultaneously occur during galvanostatic Li plating. The reaction kinetics of both processes are governed by the electronic/ionic conductivity, lithiophobicity and porosity of the interlayers. Figure 4a,b schematically shows the inside-out Li nucleation region (Fig. 4a) and outside-in Li growth region (Fig. 4b) in the mixed conductive interlayer of a Li//Li symmetric during Li plating. When an overpotential η was applied to the current collector during plating, Li nucleates in the region of the interlayer where the electrochemical overpotential is below the critical nucleation η_c ³⁵ (Fig. 4a), whereas the Li growth into the interlayer from Li anode depends on the plating capacity and porosity of interlayers as shown in Fig. 4b. The Li nucleation region and Li growth region in the interlayer can be determined quantitatively from the applied current density, plating time and properties of the interlayer (including electronic conductivity, ionic conductivity, lithiophobicity, thickness and porosity and so on) using derived equations in this work. The equations and calculation details are presented in Supplementary Note 9.

The nucleation in the interlayer substantially affected the stability of Li growth into the mixed conductive interlayer. The impact

of Li nucleation on Li plating stability of an interlayer depends on the Li nucleation length l_n , Li growth l_g and interlayer length l_i and lithiophobicity (Fig. 4a-d and Supplementary Fig. 27). In the case of the nucleation region, l_n is equal to interlayer length l_i (Supplementary Fig. 27a), and Li will also plate on the electrolyte surface, inducing SSEs reduction. If the Li growth region is smaller than the nucleation region ($l_g < l_n < l_i$; Supplementary Fig. 27b), the interlayer will gradually be penetrated by plated Li during long-term cycling because the nucleation region that was not covered by Li growth will partially stay in the interlayer as dead lithium. When the Li growth region l_g is equal to (Fig. 4c) or larger than (Fig. 4d) the nucleation region l_n but smaller than the interlayer thickness l_i , all nuclei will merge by grown Li. Well-regulated Li growth can remediate the detrimental effect of nucleation to avoid dendrite formation during cycles. This assumption has been widely verified in the field of electrochemical Li plating³⁶. For example, an anode-free lithium-metal battery could successfully cycle without lithium dendrite growth because the uneven Li nuclei on lithiophobic Cu current collector is merged by the following Li growth, which could be regulated by solid electrolyte interphase³⁶. When the Li growth region l_g is much larger than (Fig. 4d) nucleation region l_n , the lithiophobic interlayer can further stabilize the grown Li beyond the nucleation region (Figs. 4d and 2l). On the basis of the discussion above, the optimal design of mixed conductive, lithiophobic interlayers for stable Li plating/stripping is that the Li nucleation region is smaller or equal to

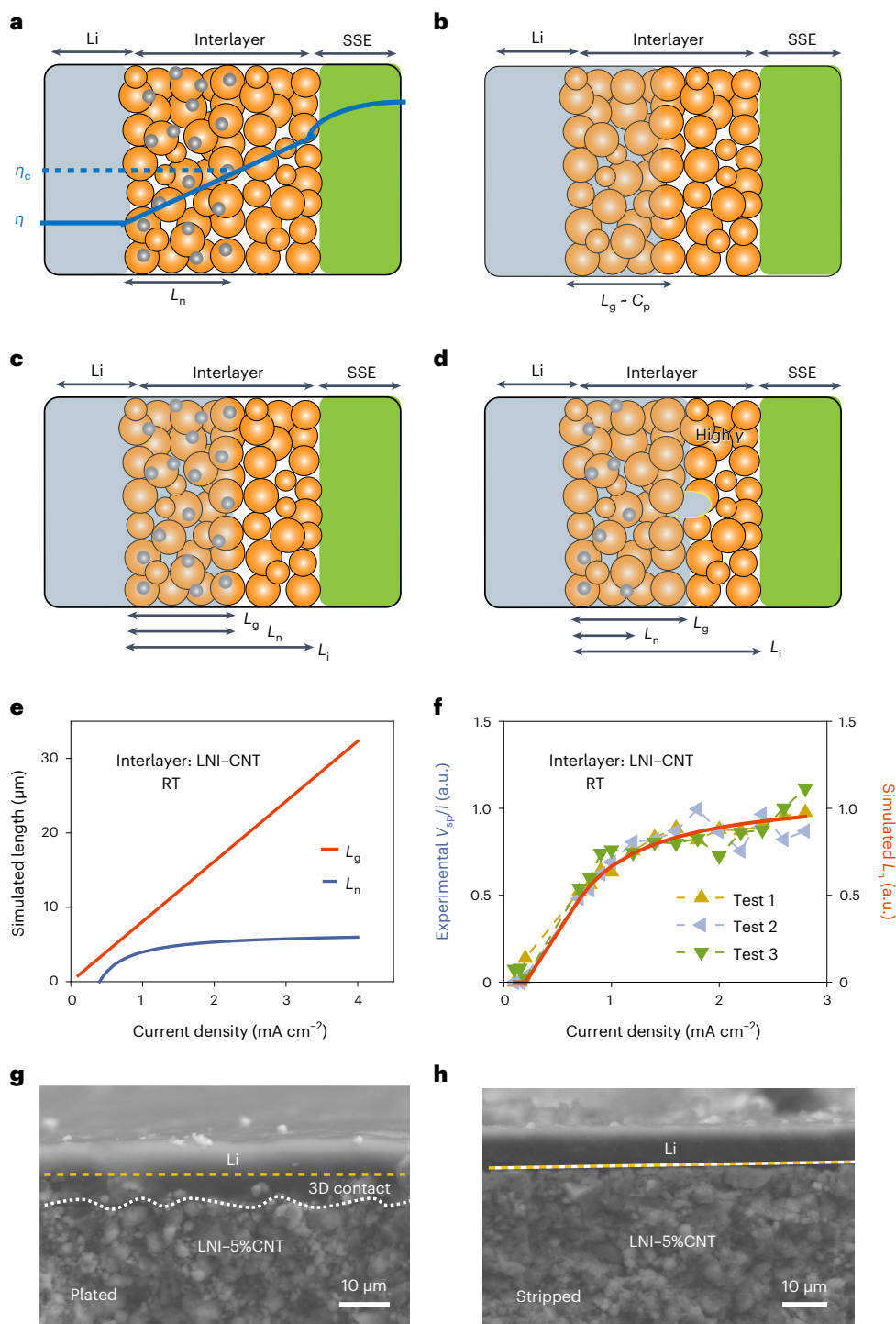


Fig. 4 | Proposed design principle for Li dendrite suppression. a, b, Definition of Li nucleation region (a) and growth region (b) in the mixed conductive interlayer of a Li//Li symmetric cell. L_n and L_g are the length of nucleation region and growth region. η , η_c and C_p represent the applied overpotential at current collector, critical Li nucleation overpotential and Li plating capacity, respectively. The solid blue line schematically shows the electrochemical potential distribution of the cell during Li plating. The dashed blue line marks the position where local Li electrochemical overpotential is equal to Li nucleation overpotential η_c . The purple balls represent the nucleated Li. The orange balls represent the particles in the interlayer. **c, d**, Schematics of mixed conductive interlayers with different Li nucleation length L_n , growth length L_g and interlayer length L_i when Li nucleation length L_n is equal to growth length L_g but is smaller

than interlayer length L_i (c) and Li nucleation length L_n is smaller than growth length L_g and interlayer length L_i (d). Li plating beyond the nucleation region will be stable if the interlayer is lithiophobic (high γ). **e**, Calculated nucleation (L_n) and growth (L_g) region for Li/LNI/Li symmetric cells with LNI-5% CNT interlayer at 25 °C. **f**, The experimentally extracted V_{sp}/i as a function of testing current density i in comparison with the simulated nucleation length in **e**. Dashed lines were added to guide the eye, whereas the red solid line is the simulation result. The standard deviation is present in Supplementary Fig. 31. **g, h**, SEM image of the Li/LNI/CNT interface in Li/LNI-CNT/LNI/LNI-CNT/Cu cell after Li plated for 2.0 mAh cm^{-2} (g) and stripped for 2.0 mAh cm^{-2} after Li plated for 4.0 mAh cm^{-2} (h). The white dotted line shows the forefront of plated Li. The yellow dotted lines show the boundary of the interlayer.

the Li growth region (Fig. 4c,d), and both lengths are slightly smaller than the interlayer thickness.

As a proof of concept, we used a 90 μm lithiophobic LNI-5% CNT interlayer to verify the interlayer design principle. We analysed the length of Li nucleation in the interlayer and Li growth into the interlayer during the galvanostatic cycling of the Li/LNI/Li cell with LNI-5% CNT interlayer after activation cycles (Fig. 3a and Supplementary Table 4). As shown in Fig. 4e, when the cell is subjected to galvanostatic Li plating/stripping at a step-increased current but a fixed charge/discharge time, the Li growth region expands almost linearly with the current because Li plating capacity increases linearly with the current (Supplementary Note 9). In contrast, Li nucleation length increased with a descent slope (Fig. 4e) because nucleation length is a linear function of the reciprocal of the current density (Supplementary Note 9). To validate nucleation length simulation (Fig. 4f), spike height voltage V_{sp} , which was defined as the voltage difference between point A and B at Supplementary Fig. 28a, was extracted from the galvanostatic cycling curve at different currents (Supplementary Figs. 28a and 29a). Due to linear distribution of electrochemical potential distribution in the mixed conductive interlayer (Supplementary Fig. 28b), the actual nucleation length l_n can be directly derived from the spike height voltage V_{sp} at the testing current density i using the equation (1) (Supplementary Note 10)

$$l_n = C \times \frac{V_{\text{sp}}}{i} \quad (1)$$

Where C is a coefficient and i is the testing current density. The spike height voltage V_{sp} at the different current density i (Supplementary Fig. 29b) was obtained from galvanostatic cycling curves (Fig. 3a and Supplementary Fig. 29). The simulated nucleation length as a function of current density has the same trend as the experimental obtained V_{sp} in three tests (Fig. 4f, Supplementary Figs. 29–31 and Supplementary Note 11), which validated the simulations.

On the basis of the Li nucleation simulation (Fig. 4e), Li does not nucleate in the LNI-5% CNT interlayer at a low current density ($<0.4 \text{ mA cm}^{-2}$) but only grows, which coincides with the absence of the sharp voltage spike in galvanostatic cycling of the Li/LNI/Li cell with LNI-5% CNT interlayer at small current density (Fig. 3a). With the increase in applied current density thus overpotential, both the Li growth length and Li nucleation length increase. During galvanostatic cycling within the current density range of $0.1\text{--}4.0 \text{ mA cm}^{-2}$, Li nucleation length in the LNI-5% CNT interlayer remains smaller than the growth length (Fig. 4e), which was also verified by SEM observations (Fig. 4g). As shown in Fig. 4g and Supplementary Fig. 32, Li plated at Li/LNI-5% CNT interface in Li/LNI-CNT/LNI/LNI-CNT/Cu cells and penetrated into porous LNI-5% CNT interlayer when Li plating capacity is 1.0 mAh cm^{-2} (Supplementary Fig. 32a), 2.0 mAh cm^{-2} (Fig. 4g) and 4.0 mAh cm^{-2} (Supplementary Fig. 32b), forming a three-dimensional Li/interlayer contact (Fig. 4g), which is consistent with the proposed mechanism in Fig. 4c,d. Upon stripping 2.0 mAh cm^{-2} of Li (Fig. 4h) from Li/LNI-5% CNT interface that was deposited for 4.0 mAh cm^{-2} (Supplementary Fig. 32b), Li inside the pore of the interlayer was extracted (Fig. 4h) but Li anode kept intimate contact with the interlayer without void formation (Fig. 4h). Therefore, a stable long-term cycling performance of $>600 \text{ h}$ has been achieved in Li/LNI/Li cells with LNI-5% CNT interlayer without short circuiting (Fig. 3c–e). In contrast, the LNI-0.5% CNT interlayer suffers from contact loss during stripping (Supplementary Fig. 33b), which accounts for its low CCD even at 60°C (Supplementary Fig. 33a).

The Li nucleation region should be smaller than the Li growth region ($l_n \leq l_g < l_i$; Fig. 4c,d), which is universal for the interlayer design. This universal interlayer design principle was further verified in LNI-5% carbon nanofiber (LNI-CNF) interlayer at room temperature and LNI-5% CNT interlayer at 60°C (Supplementary Note 12 and Supplementary Figs. 34 and 35). The proposed criteria could be used to design a mixed electronic-ionic conductive interlayer with high Li dendrite suppression capability.

Structural optimization of mixed conductive interlayers

We have analysed the Li nucleation and growth in a $90\text{-}\mu\text{m}$ -thick LNI-CNT interlayer and validated the interlayer design principle (Supplementary Table 5). To enhance the energy density of ASSLBs, the interlayer thickness should be reduced. The Li/LNI/Li symmetric cell using $14.8 \mu\text{m}$ LNI-5% CNT interlayer (Supplementary Fig. 36a) achieves a much higher CCD ($1.4 \text{ mA cm}^{-2}/1.4 \text{ mAh cm}^{-2}$; Supplementary Fig. 36b) than that with thin LNI-0.5% CNT interlayer ($0.2 \text{ mA cm}^{-2}/0.2 \text{ mAh cm}^{-2}$; Supplementary Fig. 36c) or with thin LNI-50% CNT interlayer ($0.3 \text{ mA cm}^{-2}/0.3 \text{ mAh cm}^{-2}$; Supplementary Fig. 36d) due to the mixed ionic/electronic conductivity of LNI-5% CNT interlayer. To further reduce the thickness and increase Li dendrite suppression capability of the interlayer (Fig. 5a), we propose two strategies to further restrict the Li nucleation and growth in the anode side (Fig. 5b,c) based on the interlayer design principle. One strategy is to fabricate a dual-layer mixed conductive interlayer with a more electronic conductive layer at the Li anode side and a more ionic conductive layer at the SSE side (Fig. 5b). As a proof of concept, we fabricated LNI-7% CNT/LNI-2% CNT dual-layered interlayer with a thickness of $54.5 \mu\text{m}$ (Supplementary Fig. 37). The Li dendrite suppression capability of Li/LNI/Li cell using LNI-7% CNT/LNI-2% CNT dual-layered interlayer was evaluated. As shown in Fig. 5d, a high CCD of 6.0 mA cm^{-2} with a capacity of 6.0 mAh cm^{-2} was achieved at room temperature with the total thickness of the dual-layer interlayer of $54.5 \mu\text{m}$ (Supplementary Fig. 37a), which performs much better than that of LNI-5% CNT homogeneous interlayer with a thickness of $90 \mu\text{m}$ (Fig. 3a). The drawback of the dual-layer interlayer is the complicated cell assembly process. Moreover, the thickness of the dual-layer interlayer is hard to be further reduced. To further reduce the interlayer thickness, we also fabricated a mixed ionic-electronic conductive interlayer with gradient electronic conductivity. A LNI-25% Mg interlayer with a thickness of only $18.5 \mu\text{m}$ was applied in the Li/LPSC/Li symmetric cell. Upon activation of LNI-25% Mg interlayer at 60°C , Mg in the LNI-25% Mg interlayer gradually diffuses to the Li anode side forming gradient electronic conductivity (Fig. 5e and Supplementary Fig. 38). The $18.5 \mu\text{m}$ LNI-25% Mg interlayer enabled the Li/LPSC/Li symmetric cell to stably charge/discharge at 4.0 mA cm^{-2} with a capacity of 4.0 mAh cm^{-2} for more than 100 h (Supplementary Fig. 38).

Finally, we evaluated the performances of $20 \mu\text{m}$ -Li/LPSC/LSO@NMC811 full cells with LNI-5% CNT and LNI-25% Mg interlayer at 60°C (Fig. 5f,g and Supplementary Table 6). Twenty μm -Li/LPSC/LSO@NMC811 full cells without Li metal interlayer were also fabricated for comparison. The Li/LNI-5% CNT/LPSC/LSO@NMC811 provides a discharge-specific capacity of 191.6 mAh g^{-1} in the first cycle and maintains a discharge capacity of 147.0 mAh g^{-1} after 180 cycles. In contrast, Li/LPSC/LSO@NMC811 full cells without interlayer were softly short circuited after only five cycles (Supplementary Fig. 39). Figure 5f shows the charge/discharge curves of Li/LNI-Mg/LPSC/LSO@NMC811 cell at the current density of 1.1 mA cm^{-2} between 2.7 and 4.3 V at 60°C . Twenty μm -Li/LPSC/LSO@NMC811 with LNI-25% Mg interlayer has a much higher capacity retention of 82.4% after the 350 cycles (Fig. 5g). The better performance of Li/LPSC/LSO@NMC811 full cells with LNI-Mg than that without Mg is due to better controlled Li plating sites (Fig. 5c), higher Li diffusivity in Li-Mg alloy³⁷ and reduced side reaction between interlayer and LPSC electrolyte (Supplementary Fig. 40 and Supplementary Note 13). The successful demonstration of the Li//NMC811 cell using LNI-CNT interlayer and LNI-Mg interlayer indicates that our design principle can be used to design a mixed ionic-electronic conductive interlayer with high lithium dendrite suppression capability.

Conclusions

In this work, we developed an interlayer design principle for Li dendrite suppression in ASSLBs by considering both Li nucleation inside the interlayer and Li growth from the Li anode into the interlayer. Guided by theoretical simulation and experimental validation of the interlayer

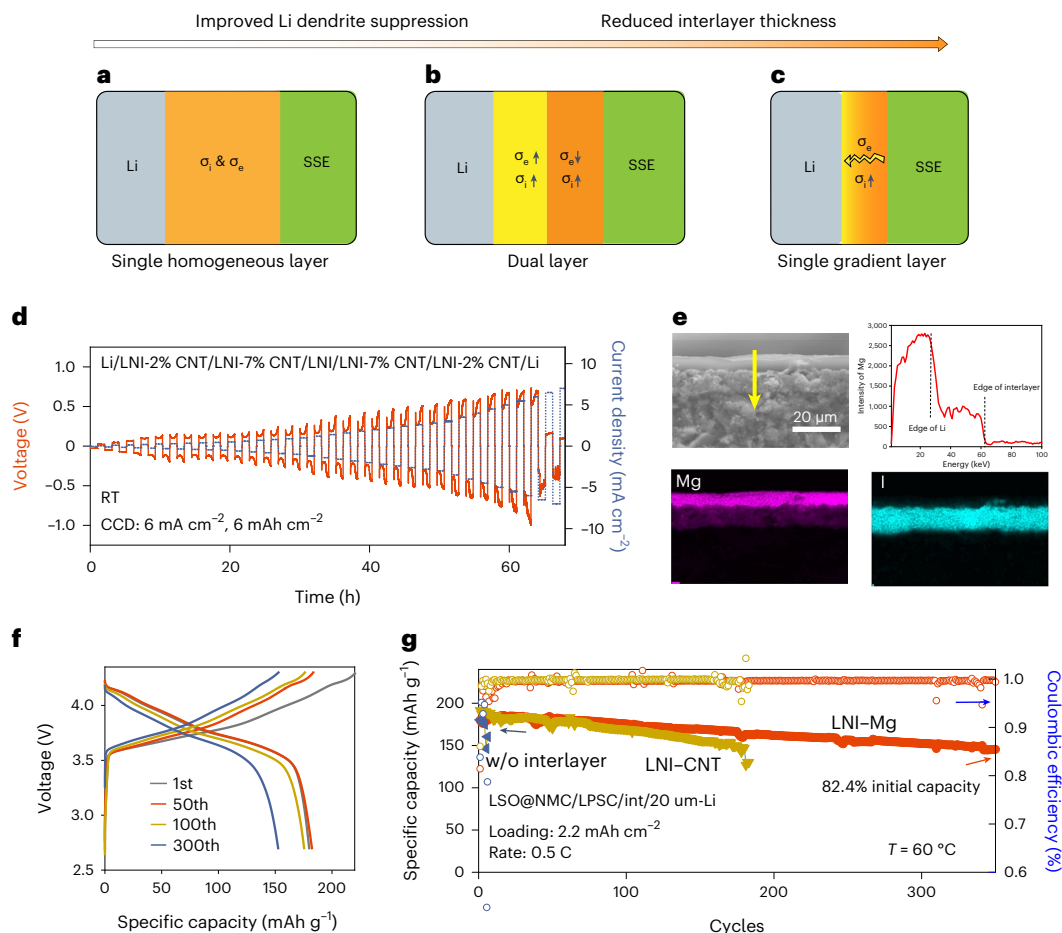


Fig. 5 | Optimization of mixed conductive interlayer and full cell performance with a 20 μm lithium-metal anode. **a–c**, Schematic of optimization strategies for mixed ionic–electronic conductive interlayer to minimize the interlayer thickness and improve Li dendrite suppression capability. The performance is single homogeneous layer < double layer < gradients layer. **d**, Galvanostatic cycling of Li/LNI-7% CNT/LNI-2% CNT/LNI/LNI-2% CNT/LNI-7% CNT/Li cells at step-increased current densities at 25 $^{\circ}\text{C}$. **e**, SEM, Mg element line scan and

elemental mapping of activated Li/LNI-Mg interface in Li/LNI-Mg/LPSC/Li cells. **f**, Charge–discharge curves of the Li/LNI-Mg/LPSC/LSO@NMC811 full cell at 60 $^{\circ}\text{C}$. **g**, Cycling performance of solid-state LSO@NMC811/LPSC/int/20 μm -Li full cell (int = LNI-CNT or LNI-Mg) at a rate of 0.5 C with an areal capacity of 2.2 mAh cm^{-2} . LSO@NMC811/LPSC/20 μm -Li full cell was used as a reference. w/o represents without.

design principle, we designed a porous and lithiophobic mixed ionic/electronic conductive LNI-CNT interlayer and electronic conduction gradient LNI-Mg interlayer between solid electrolyte and Li metal. The LNI-CNT interlayer with a high ionic conductivity but a low electronic conductivity and high lithiophobicity enables Li//Li symmetric cell with LNI electrolyte to achieve a high critical current density of 4.0 mA cm^{-2} at a capacity of 4.0 mAh cm^{-2} at room temperature. The LNI-Mg interlayer with gradient electronic conduction enables LSO@NMC811/LPSC/Li full cell with an areal capacity of 2.2 mAh cm^{-2} to maintain 82.4% of the capacity after 350 cycles at 60 $^{\circ}\text{C}$. The proposed interlayer design principles provide a pathway to develop safer and higher energy ASSLBs.

Methods

Sample Preparations

The $\text{Li}_7\text{N}_2\text{I}$ (LNI) powder was prepared by ball milling and sintering methods as reported previously³⁸. First, lithium nitride (Li_3N , Sigma-Aldrich, purity 99.5%) and lithium iodide (LiI, Sigma-Aldrich, purity 99.9%) with a molar ratio of 2:1 were ball milled (PM 100, Retsch) at 400 r.p.m. for 12 h in an argon-filled atmosphere. The mill rotated for 10 min in one direction, rested for 5 min and then rotated in the reverse direction for 10 min to reduce the temperature elevation during ball milling. After that, 100 mg of milled powder was pressed using a pressing die with an inner diameter of 10 mm at 360 MPa for 5 min. The obtained pellets were placed in a molybdenum crucible and transferred to a

tube furnace quickly. A yellow dense pellet was obtained after heating at 550 $^{\circ}\text{C}$ for 2 h with a heating rate of 5 $^{\circ}\text{C}$ under N_2 atmosphere. The pellet was ground with agate mortar by hand and screened with 400 mesh sieves. The LNI- x wt% carbon ($x = 0, 0.5, 5, 50$) mixture was prepared by milling the corresponding chemicals for 15 minutes in Ar atmosphere. The LNI-Mg sample was prepared by milling the LNI with 25 wt% Mg powder. To avoid the contamination of H_2O and O_2 , all sample handling was conducted in an Ar-filled glovebox (MBRAUN).

Li_4SiO_4 -coated NMC811 cathode was prepared in the lab. Typically, 3.1 mg of Li drops into 1.2 ml of ethyl alcohol (EtOH, Sigma-Aldrich, 99%) until fully dissolved. The solution was mixed with 50 μl of tetraethyl orthosilicate (TEOS, Sigma-Aldrich, 98%) and stirred at 300 r.p.m. for 10 minutes. Then, 1 g of NMC811 cathode was added to the solution and stirred at 300 r.p.m. for 60 minutes. The suspension was sonicated in the vacuum to remove the solvent. The final clay was calcinated at 350 $^{\circ}\text{C}$ for 2 h in the O_2 atmosphere.

Structural characterization

X-Ray diffraction analysis was conducted in a D8 Advance diffractometer (Bruker) equipped with $\text{Cu K}\alpha$ radiation at 40 kV, 40 mA. The 2θ range is 10–80 $^{\circ}$ with 0.2 $^{\circ}$ step increments. The powder samples were protected with Scotch tape to prevent contamination by air and moisture. Raman spectra were performed in a Jobin-Yvon LabRAM HR Raman spectrometer. The measurements were performed by using

the green line of an argon ion laser ($\lambda = 514.5$ nm) with a resolution of 1 cm^{-1} . The morphologies and element distribution of LNI–CNT composite interlayers were obtained on a field-emission scanning electron microscope (SEM, SU-70, Hitachi) equipped with an energy dispersive X-ray detector. Conductive Cu tape was used to analyse the element distribution of carbon-containing samples. The distribution of lithium element in the cycled LNI–CNT interlayer was analysed by time-of-flight secondary ion mass spectrometry (ToF-SIMS) attached with the Ga^+ focused-ion beam/SEM (Tescan GAIA3). The accelerated voltage for focused-ion beam/SEM was 10 kV. X-ray photoelectron spectroscopy (XPS) was conducted on a high-sensitivity Kratos AXIS 165 X-ray photoelectron spectrometer using Mg K α radiation. Binding energy values were referenced to the $\text{Cl}2p$ peak at 198.8 eV to avoid the influence of the carbon element in the samples. The CasaXPS software was used to fit the XPS spectra.

The sessile drop technique was used to measure the contact angle of liquid lithium on LNI, carbon and LNI–carbon surfaces, as described previously³⁹. High-purity lithium (Sigma-Aldrich, 99%) was employed for the tests. The clean LNI, carbon and LNI–carbon samples were heated on a hot plate in an Ar-protected glovebox to the desired temperatures. Then, drops of liquid Li were transferred to the surface of the samples using a glass pipette. The contact angle measurement tests were carried out at temperatures of 300 °C with a holding time of 60 min.

The relative density of pressed LNI–CNT pellets was measured by the Archimedes method at room temperature using the Mettler Toledo Density Kit. To determine the density of LNI–CNT pellets, the weights of a pellet were measured both in the air and immersed in the mineral spirits. Because the density of air ($\rho_{\text{air}} = 0.0012\text{ g ml}^{-1}$) and mineral spirits ($\rho_{\text{ms}} = 0.752\text{ g ml}^{-1}$) are different, the weights of a pellet in the air m_{air} and in the mineral spirits m_{ms} should be different due to different buoyancy. The density of the pellet can be calculated by

$$\rho = \frac{m_{\text{air}}}{m_{\text{air}} + m_{\text{ms}}} \times (\rho_{\text{ms}} - \rho_{\text{air}}) + \rho_{\text{air}} \quad (2)$$

The density of each sample was collected for three times and normalized by the theoretical density of LNI crystal (2.38 g cm^{-3}) to get the relative density.

Electrochemical measurements

The electrochemical stability of LNI was evaluated by the linear scan voltammetry with an asymmetric cell using carbon black and solid electrolytes composites as the working electrode and lithium metal as the counter/reference electrode. The open circuit voltage is 0.9 V. The voltage range is from 0.9–2.0 V and the scan rate is 0.1 mV s^{-1} .

The total conductivity of LNI–*x*% carbon samples were carried out on an electrochemical station (Gamry G1000) with sputtered Au as the electrode. The measurements were performed over the frequency range from 0.1 Hz to 1 MHz. The a.c. voltage amplitude was 10 mV. For electronic conductivity measurement, the same cell configuration was used under d.c. voltages of 0.1 V. Ionic conductivity of LNI–50% CNT was obtained from d.c. polarization of Li/LPSC/LNI–50% CNT/LPSC/Li cell. The applied constant voltage is 50 mV. The weight of $\text{Li}_6\text{PS}_5\text{Cl}$ in each side is 50 mg and the resistance contribution from $\text{Li}_6\text{PS}_5\text{Cl}$ in both side was estimated to be 100 Ω and was deducted for the calculation of ionic conductivity. The ZView4 programme was used to fit the impedance spectra.

Li/SSEs/Li symmetric cell assembly

To assemble the Li/SSEs/Li all-solid-state cell, 70 mg LNI solid electrolyte powder was pressed into a pellet under 360 MPa in a pellet mould with a diameter of 0.5 inch. After that, 3–15 mg LNI–*x*%-CNT or LNI–25%-Mg composite was put on both sides of the solid electrolyte and pressed into a pellet. After that, two Li discs with a diameter of 8 mm were attached on both sides of the solid electrolyte. The galvanostatic cycling test was determined by a Land test system (CT2001A).

To measure the nucleation overpotential of Li on interlayer, the Li/interlayer/electrolyte/interlayer/stainless steel cell was assembled by attaching one Li disc to one side of the cells. Li/LNI–CNT/LNI/LNI–CNT/Cu cell was assembled by attaching Li to one side of the cell and Cu foil to the other side. Li plates to the Cu side at a current density of 0.5 mA cm^{-2} with capacity of 1 mAh cm^{-2} , 2 mAh cm^{-2} and 4 mAh cm^{-2} and then stripped with capacity of 2 mAh cm^{-2} at 60 °C. The Cu was peeled off and Li/interlayer interface was observed using SEM. The interlayer mass and actual applied current of Li//Li cell in the work are present in Supplementary Table 5.

Li/NMC811 full cell assembly

Li_4SiO_4 -coated NMC811 (LSO@NMC) was mixed with LPSC and carbon black (SAFT, C65) with the weight ratio of 70:27:3 as composite cathode material. To assemble the Li/LNI–5% CNT/LPSC/NMC811 all-solid-state full cells, 100 mg of LPSC electrolyte was first pressed at 180 MPa to form an electrolyte pellet. The thickness of the electrolyte pellet is 600 μm . Then, 20 mg of composite cathode powder was spread on one side of the electrolyte and LNI–5% CNT mixture on the other side and pressed on 360 MPa for 10 minutes. Finally, 20 μm -Li foil was attached to the LNI–5% CNT mixture side of the electrolyte pellet. The area of the electrode is 1.13 cm^2 . Li/LNI–25% Mg/LPSC/NMC811 all-solid-state full cells were assembled in the same methods as Li/LNI–5% CNT/LPSC/NMC811 cells. The assembled cells were rested at 60 °C for 12 h to allow Mg diffusion from interlayer to anode. The stack pressure for the full cell was -1 MPa . Twenty μm -Li/LPSC/NMC811 all-solid-state full cells without interlayer were also assembled for comparison. The cathode loading and actual applied current parameters of full cell are listed in Supplementary Table 6.

Li^+ conduction properties of LNI

Ab initio calculations based on density functional theory using the Perdew–Burke–Ernzerhof realization of the generalized gradient approximation for the exchange correlation was performed, as implemented in the Vienna Ab initio Simulation Package (VASP 6.3.0)^{40,41}. All atoms were relaxed fully until the force on them was less than 0.05 eV \AA^{-1} . The kinetic energy cut-off was set above 520 eV. The Brillouin zone is sampled by using the Monkhorst–Pack scheme. The voltage plateaus were obtained using the calculated density functional theory energies of all the relevant compounds in the Li–N–I space, which were obtained from the Materials Project⁴². The Li probability density isosurface of LNI was calculated from the ab initio molecular dynamic simulation. A plane wave energy cut-off of 400 eV was chosen and a minimal Γ -centred $1 \times 1 \times 1$ *k*-point grid was used. The initial structures were statically relaxed and were set to an initial temperature of 10 K. The structures were then heated to targeted temperatures (800 K) at a constant rate by velocity scaling over a time period of 3 ps. The constant-temperature, constant-volume ensemble (NVT) ensemble using a Nosé–Hoover thermostat was adopted⁴³. Li probability density isosurface was extracted by using pymatgen package and visualized in VESTA. The isosurface level is set as 0.002.

Topological analysis of LNI lattice was performed on ToposPro 5.4 software⁴⁴. The voids and channels for the N_2I^{7-} sublattice was built by running Dirichlet and ignoring Li atoms. The channel is assumed to be inaccessible for Li^+ ions if the sum of radii of the Li ion and the framework atom (N^{3-} or I^-) exceeds the channel radius by more than 10% (2.0 Å). All the voids that are smaller than the Li^+ radius (0.9 Å) and all the channel that is inaccessible for Li^+ ions were excluded. The accessible channel and void are plotted with a solid yellow stick in Supplementary Fig. 2.

Li ion and electron transport in mixed conductive interlayer

The Li ion and electron transport models for ionic conductive, electronic conductive and mixed conductive interlayers were set up using COMSOL 5.6 Multiphysics software. Nernst–Planck equations based on mass conservation was used to describe the migration of electron and Li ion at the interlayer⁴⁵.

$$\frac{\partial c_i}{\partial x} + \nabla \times J_i = R_i \quad (3)$$

$$J_i = -D_i \nabla c_i - u_{m,i} F c_i \nabla V \quad (4)$$

Where i is electron or Li ion. c_i is the local concentration of species. J_i is the species flux. R_i is the local reaction rate. D_i is the chemical diffusivity of species. $u_{m,i}$ is the species mobility, which is determined by the Nernst–Einstein relation as in equation (5).

$$u_{m,i} = \frac{D_i}{RT} \quad (5)$$

Here R is ideal gas constant and T is the temperature. Then, Poisson's equation was coupled to simulate charge separation that typically arises close to an electrode surface⁴⁶.

$$\nabla \times D = \rho_V \quad (6)$$

Where D is the electric displacement, ρ_V is the volumetric charge density. Electric displacement is determined by the following equation.

$$D = \varepsilon \times E \quad (7)$$

$$E = -\nabla V \quad (8)$$

Where ε is the permittivity, E is the electric field intensity and V is the electric potential. The electron and Li ion distribution after 2 seconds of evolution from initial state were used for Li nucleation and growth rate analysis. The local Li growth rate was determined as²⁹

$$i = i_0 \times \left(\frac{c_{\text{Li}^+}^{\text{local}}}{c_{\text{Li}^+}^0} \frac{c_{\text{e}^-}^{\text{local}}}{c_{\text{e}^-}^{\text{Li}}} \times \exp\left(\frac{-\alpha F \varphi}{RT}\right) - \exp\left(\frac{(1-\alpha) F \varphi}{RT}\right) \right) \quad (9)$$

i_0 is the exchange current density of Li plating reaction. $c_{\text{Li}^+}^0$ is the standard Li^+ concentration, equal to 1 mol l^{-1} . $c_{\text{e}^-}^{\text{Li}}$ is the electron concentration of Li metal. $c_{\text{Li}^+}^{\text{local}}$ and $c_{\text{e}^-}^{\text{local}}$ are the local Li^+ and electron concentration at the Li growth site.

The local Li nucleation rate was determined based on classical nucleation theory^{28,30}

$$J = J_0 \times \frac{c_{\text{Li}^+}^{\text{local}}}{c_{\text{Li}^+}^0} \frac{c_{\text{e}^-}^{\text{local}}}{c_{\text{e}^-}^{\text{Li}}} \times \exp\left(-\Delta G_{\text{hom}} \times \kappa_{\text{het}}\right) \quad (10)$$

where J_0 is the maximum nucleation rate. On the basis of classical nucleation theory, homogeneous nucleation barrier $\Delta G_{\text{hom}} = \frac{16\pi\gamma^3 \times V_m^2}{3(\eta F)^2 RT}$.

Here γ is the surface energy of Li metal, V_m is the molar volume of Li metal, η is the applied overpotential, F is the Faraday's constant and κ_{het} is the heterogeneous nucleation coefficient, which is equal to $\frac{2-3\cos\theta+(\cos\theta)^3}{4}$ and $\cos\theta$ is the contact angle of Li on substrate. Because the interlayer is porous, inertial and mechanical forces of Li are not incorporated^{47,48}. The ionic conductive, electronic conductive and mixed conductive interlayers are differentiated by free electron concentration and diffusivity, which were extracted from experimental data. The utilized parameters for the model were listed in Supplementary Tables 1 and 2.

Li growth by phase field method

To simulate Li plating in lithiophobic electrolyte, chemical energy, interfacial energy and electrochemical energy were considered in a phase field model⁴⁹ as in equation (11).

$$f = f_{\text{chem}} + f_{\text{intf}} + f_{\text{elec}} \quad (11)$$

The chemical energy term is formulated as a double well function.

$$f_{\text{chem}} = A \times \zeta^2 \times (1 - \zeta)^2 + \frac{B}{2} \zeta^2 \phi_g^2 \quad (12)$$

Here ζ is phase field parameter of Li metal phase ($\zeta = 1$ for Li metal), ϕ_g is the phase field parameter for electrolyte ($\phi_g = 1$ for electrolyte). A and B were the barrier height of phase transition. The interfacial term is a function of order parameter gradient.

$$f_{\text{intf}} = \frac{1}{2} k_\zeta (\nabla \zeta)^2 - k_{\text{Li-grain}} \sum_{g=1}^N \nabla \zeta \nabla \phi_g + \frac{1}{2} k_\phi (\nabla \phi_g)^2 \quad (13)$$

Where k_ζ and k_ϕ are the gradient coefficient associate with surface energy of Li metal and solid electrolyte. $k_{\text{Li-grain}}$ is associated with the interfacial energy between Li metal and solid electrolyte. The electrochemical term is related to local potential as

$$f_{\text{elec}} = F \times \varphi \times c_{\text{Li}^+} \quad (14)$$

Therefore, the total energy can be expressed as:

$$f = A \times \zeta^2 (1 - \zeta)^2 + \frac{B}{2} \zeta^2 \phi_g^2 + \frac{1}{2} k_\zeta (\nabla \zeta)^2 - k_{\text{Li-grain}} \sum_{g=1}^N \nabla \zeta \nabla \phi_g + \frac{1}{2} k_\phi (\nabla \phi_g)^2 + F \times \varphi \times c_{\text{Li}^+} \quad (15)$$

The governing equation for the phase field model is the Allen–Cahn equation⁴⁹.

$$\frac{\partial \zeta}{\partial t} = -L_\sigma \left(\frac{\partial f_0}{\partial \zeta} - k_\zeta \nabla^2 \left(\zeta - \frac{k_{\text{Li-grain}}}{k_\zeta} \phi_g \right) \right) - L_\eta R T h'(\zeta) \left(\exp\left(\frac{(1-\alpha)F\eta}{RT}\right) - \frac{c_{\text{Li}^+}}{c_0} \exp\left(-\frac{\alpha F \eta}{RT}\right) \right) \quad (16)$$

Here t is time, ζ is the phase field parameter for Li, L_σ is interfacial mobility, f_0 is total energy, k_ζ is the interfacial coefficient, L_η is the electrochemical reaction constant, $h'(\zeta) = 30 \times \zeta^2 (1 - \zeta)^2$, α is the symmetry factor of Li deposition/stripping reaction, F is the Faraday's constant, R is the ideal gas constant and η is the applied potential. The utilized parameters for the phase field model were listed in Supplementary Table 3.

Data availability

The data supporting the findings of this study are available within the article and its Supplementary Information files.

References

- Larcher, D. & Tarascon, J.-M. Towards greener and more sustainable batteries for electrical energy storage. *Nat. Chem.* **7**, 19–29 (2015).
- Nunes, A., Woodley, L. & Rossetti, P. Re-thinking procurement incentives for electric vehicles to achieve net-zero emissions. *Nat. Sustain.* **5**, 527–532 (2022).
- Janek, J. & Zeier, W. G. A solid future for battery development. *Nat. Energy* **1**, 16141 (2016).
- Famprikis, T., Canepa, P., Dawson, J. A., Islam, M. S. & Masquelier, C. Fundamentals of inorganic solid-state electrolytes for batteries. *Nat. Mater.* **18**, 1278–1291 (2019).
- Bates, A. M. et al. Are solid-state batteries safer than lithium-ion batteries? *Joule* **6**, 742–755 (2022).
- He, X. et al. The passivity of lithium electrodes in liquid electrolytes for secondary batteries. *Nat. Rev. Mater.* **6**, 1036–1052 (2021).
- Monroe, C. & Newman, J. The impact of elastic deformation on deposition kinetics at lithium/polymer interfaces. *J. Electrochem. Soc.* **152**, A396 (2005).

8. Wang, Y., Dang, D., Wang, M., Xiao, X. & Cheng, Y. T. Mechanical behavior of electroplated mossy lithium at room temperature studied by flat punch indentation. *Appl. Phys. Lett.* **115**, 043903 (2019).
9. Cao, D. et al. Lithium dendrite in all-solid-state batteries: growth mechanisms, suppression strategies, and characterizations. *Matter* **3**, 57–94 (2020).
10. Swamy, T. et al. Lithium metal penetration induced by electrodeposition through solid electrolytes: example in single-crystal $\text{Li}_6\text{La}_3\text{ZrTaO}_{12}$ garnet. *J. Electrochem. Soc.* **165**, A3648–A3655 (2018).
11. Liu, H. et al. Controlling dendrite growth in solid-state electrolytes. *ACS Energy Lett.* **5**, 833–843 (2020).
12. Han, F. D. et al. High electronic conductivity as the origin of lithium dendrite formation within solid electrolytes. *Nat. Energy* **4**, 187–196 (2019).
13. Liu, X. et al. Local electronic structure variation resulting in Li ‘filament’ formation within solid electrolytes. *Nat. Mater.* **20**, 1485–1490 (2021).
14. Raj, V. et al. Direct correlation between void formation and lithium dendrite growth in solid-state electrolytes with interlayers. *Nat. Mater.* **21**, 1050–1056 (2022).
15. Han, F. D., Zhu, Y., He, X., Mo, Y. & Wang, C. Electrochemical stability of $\text{Li}_{10}\text{GeP}_2\text{S}_{12}$ and $\text{Li}_7\text{La}_3\text{Zr}_2\text{O}_{12}$ solid electrolytes. *Adv. Energy Mater.* **6**, 1501590 (2016).
16. Wang, S. et al. Lithium chlorides and bromides as promising solid-state chemistries for fast ion conductors with good electrochemical stability. *Angew. Chem. Int. Ed.* **58**, 8039–8043 (2019).
17. Shen, F., Dixit, M. B., Xiao, X. & Hatzell, K. B. Effect of pore connectivity on Li dendrite propagation within LLZO electrolytes observed with synchrotron X-ray tomography. *ACS Energy Lett.* **3**, 1056–1061 (2018).
18. Venturi, V. & Viswanathan, V. Thermodynamic analysis of initial steps for void formation at lithium/solid electrolyte interphase interfaces. *ACS Energy Lett.* **7**, 1953–1959 (2022).
19. Tsai, C.-L. et al. $\text{Li}_7\text{La}_3\text{Zr}_2\text{O}_{12}$ interface modification for Li dendrite prevention. *ACS Appl. Mater. Interfaces* **8**, 10617–10626 (2016).
20. Han, X. et al. Negating interfacial impedance in garnet-based solid-state Li metal batteries. *Nat. Mater.* **16**, 572–579 (2017).
21. Wang, C. et al. Universal soldering of lithium and sodium alloys on various substrates for batteries. *Adv. Energy Mater.* **8**, 1701963 (2018).
22. Tian, Y. et al. $\text{Li}_{6.75}\text{La}_3\text{Zr}_{1.75}\text{Ta}_{0.25}\text{O}_{12}$ @amorphous Li_3OCl composite electrolyte for solid state lithium-metal batteries. *Energy Storage Mater.* **14**, 49–57 (2018).
23. You, Y. et al. Effect of charge non-uniformity on the lithium dendrites and improvement by the LiF interfacial layer. *ACS Appl. Energy Mater.* **5**, 15078–15085 (2022).
24. Ji, X. et al. Solid-state electrolyte design for lithium dendrite suppression. *Adv. Mater.* **32**, 2002741 (2020).
25. Wang, T. et al. A self-regulated gradient interphase for dendrite-free solid-state Li batteries. *Energy Environ. Sci.* **15**, 1325–1333 (2022).
26. Lee, Y.-G. et al. High-energy long-cycling all-solid-state lithium metal batteries enabled by silver–carbon composite anodes. *Nat. Energy* **5**, 299–308 (2020).
27. Biswal, P., Stalin, S., Kludze, A., Choudhury, S. & Archer, L. A. Nucleation and early stage growth of Li electrodeposits. *Nano Lett.* **19**, 8191–8200 (2019).
28. Jo, S. et al. The roles of nucleation and growth kinetics in determining Li metal morphology for Li metal batteries: columnar versus spherical growth. *J. Mater. Chem. A* **10**, 5520–5529 (2022).
29. Dickinson, E. J. F. & Wain, A. J. The Butler–Volmer equation in electrochemical theory: origins, value, and practical application. *J. Electroanal. Chem.* **872**, 114145 (2020).
30. Pei, A., Zheng, G., Shi, F., Li, Y. & Cui, Y. Nanoscale nucleation and growth of electrodeposited lithium metal. *Nano Lett.* **17**, 1132–1139 (2017).
31. Suzuki, N. et al. Highly cyclable all-solid-state battery with deposition-type lithium metal anode based on thin carbon black layer. *Adv. Sustain. Syst.* **11**, 2100066 (2021).
32. Kim, S. et al. High-power hybrid solid-state lithium–metal batteries enabled by preferred directional lithium growth mechanism. *ACS Energy Lett.* **8**, 9–20 (2023).
33. Wang, C. et al. Identifying soft breakdown in all-solid-state lithium battery. *Joule* **6**, 1770–1781 (2022).
34. Rebelo, S. L. H. et al. Progress in the Raman spectra analysis of covalently functionalized multiwalled carbon nanotubes: unraveling disorder in graphitic materials. *Phys. Chem. Chem. Phys.* **18**, 12784–12796 (2016).
35. Guan, X. et al. Controlling nucleation in lithium metal anodes. *Small* **14**, 1801423 (2018).
36. Huang, C. J. et al. Decoupling the origins of irreversible coulombic efficiency in anode-free lithium metal batteries. *Nat. Commun.* **12**, 1452 (2021).
37. Krauskopf, T., Mogwitz, B., Rosenbach, C., Zeier, W. G. & Janek, J. Diffusion limitation of lithium metal and Li–Mg alloy anodes on LLZO-type solid electrolytes as a function of temperature and pressure. *Adv. Energy Mater.* **9**, 1902568 (2019).
38. Obayashi, H., Gotoh, A. & Nagai, R. Composition dependence of lithium ionic conductivity in lithium nitride–lithium iodide system. *Mat. Res. Bull.* **16**, 581–585 (1981).
39. Lu, X. et al. Liquid–metal electrode to enable ultra-low temperature sodium–beta alumina batteries for renewable energy storage. *Nat. Commun.* **5**, 4578 (2014).
40. Kresse, G. & Furthmüller, J. Efficient iterative schemes for ab initio total-energy calculations using a plane-wave basis set. *Phys. Rev. B* **54**, 11169 (1996).
41. Perdew, J. P., Ernzerhof, M. & Burke, K. Rationale for mixing exact exchange with density functional approximations. *J. Chem. Phys.* **105**, 9982–9985 (1996).
42. Jain, A. et al. Commentary: the materials project: a materials genome approach to accelerating materials innovation. *APL Mater.* **1**, 011002 (2013).
43. Nose, S. Constant temperature molecular dynamics methods. *Prog. Theor. Phys. Suppl.* **103**, 1–46 (1991).
44. Blatov, V. A., Shevchenko, A. P. & Proserpio, D. M. Applied topological analysis of crystal structures with the program package ToposPro. *Cryst. Growth Des.* **14**, 3576–3586 (2014).
45. Meng, D., Zheng, B., Lin, G. & Sushko, M. L. Numerical solution of 3D Poisson–Nernst–Planck equations coupled with classical density functional theory for modeling ion and electron transport in a confined environment. *Commun. Comput. Phys.* **16**, 1298–1322 (2014).
46. Wang, H., Thiele, A. & Pilon, L. Simulations of cyclic voltammetry for electric double layers in asymmetric electrolytes: a generalized modified Poisson–Nernst–Planck model. *J. Phys. Chem. C* **117**, 18286–18297 (2013).
47. Sommer, J. L. & Mortensen, A. Forced unidirectional infiltration of deformable porous media. *J. Fluid Mech.* **31**, 193–217 (1996).
48. Brinkman, H. C. A calculation of the viscous force exerted by a flowing fluid on a dense swarm of particles. *Flow Turbul. Combust.* **1**, 27–34 (1949).
49. Chen, L. et al. Modulation of dendritic patterns during electrodeposition: a nonlinear phase-field model. *J. Power Sources* **300**, 376–385 (2015).

Acknowledgements

This work was supported by the US Department of Energy (DOE) under award number DEEE0008856 (received by C.W.) and award number DE-AC05-76RL01830.

Author contributions

Z.W. designed and conducted the experiments, performed the calculations and analysed the data. J.X., X.J. and H.W. conducted the electrochemical experiments. J.X., J.Z. X.H. and W.Z. performed XRD, Raman, SEM and ToF-SIMS characterizations. Y.L. synthesized the LLZO. Z.W. wrote the draft manuscript. All authors revised the manuscript. C.W. conceived and supervised the project. All authors contributed to the interpretation of the results.

Competing interests

The authors declare no competing interests.

Additional information

Supplementary information The online version contains supplementary material available at <https://doi.org/10.1038/s41560-023-01426-1>.

Correspondence and requests for materials should be addressed to Hongli Wan or Chunsheng Wang.

Peer review information *Nature Energy* thanks Nagaphani Aetukuri, Nicolas Delaporte and the other, anonymous, reviewer(s) for their contribution to the peer review of this work.

Reprints and permissions information is available at www.nature.com/reprints.

Publisher's note Springer Nature remains neutral with regard to jurisdictional claims in published maps and institutional affiliations.

Springer Nature or its licensor (e.g. a society or other partner) holds exclusive rights to this article under a publishing agreement with the author(s) or other rightsholder(s); author self-archiving of the accepted manuscript version of this article is solely governed by the terms of such publishing agreement and applicable law.

© The Author(s), under exclusive licence to Springer Nature Limited 2024